Microstructurally related model for predicting behaviour of unsaturated soils with double porosity in triaxial space

Tianchi Wu[1], Guoqing Cai[2], Peter Cleall[3], Snehasis Tripathy[4]

[1]Ph.D. student, School of Engineering, Cardiff University, Cardiff, United Kingdom

[2]Professor, School of Civil Engineering, Beijing Jiaotong University, Beijing, China.

Corresponding author Email: guoqing.cai@bjtu.edu.cn

[3]Professor, School of Engineering, Cardiff University, Cardiff, United Kingdom.

[4]Professor, School of Engineering, Cardiff University, Cardiff, United Kingdom.

ABSTRACT

Microstructure can have an important impact on the hydraulic and mechanical behaviour of unsaturated soil and so it is necessary for it to be considered in constitutive models to enable accurate predictions of soil behaviour. This paper focuses on constitutive modelling of soils exhibiting a dual-porosity structure. Based on the assumption that macro and micropores contained in the double porosity structure have different influences on the mechanical and hydraulic behaviour, the effective degree of saturation was selected as a microstructural index. This microstructural index was implemented within a Bishop's effective stress based approach and the Glasgow Coupled Model and the Modified Camclay Model were adopted as the basic framework for the development of a constitutive model. Typical samples of low-expansive, non-expansive and collapsible soils with dual porosity were selected to validate the model's

performance, with the model found to perform well when compared with experimental data in terms of isotropic compression, triaxial shear and wetting tests.

Key words: unsaturated soils; coupled constitutive model; effective degree of saturation; microstructure

INTRODUCTION

Recently, there has been growing interest in how the microstructure affects the hydraulic and mechanical behaviour of unsaturated soils (Cai et al. 2014, 2020b; a; Cuisinier et al. 2011; Jia et al. 2020; Low et al. 2008; Manahiloh et al. 2016; Ranaivomanana et al. 2017; Romero and Simms 2008; Sánchez et al. 2016; Sergeyev et al. 1980; Tian-er and Lin 2010; Trzciński and Wójcik 2019). The microstructure can be classified as having single or double porosity (Alazaiza et al. 2017; Bagherieh et al. 2009; Russell 2010) according to features of pore size distribution (PSD). The PSD for double porosity manifests significant bimodality, which is related to the presence of both macro and micropores (Casini et al. 2012; Lewandowska et al. 2004; Musso et al. 2014; Ngien et al. 2012). According to Li et al (2019), the macropores are mainly deformed during loading while the micropores are less affected; however, during drying and wetting process, the micropores will exhibit significant changes and be accompanied by reversible volumetric deformation.

A review of the literature (Cai et al. 2018; Li et al. 2013, 2019; Mašín 2013; Mašín et al. 2005) suggests that there are two ways to consider the effects of double porosity on the hydraulic and mechanical behaviour of unsaturated soils. The first way is

adopting a specific microstructural index to represent the main features of double porosity. For example, the effective degree of saturation can be adopted as this index considers the different impacts of water within macropores and micropores, which provides an indirect way to take features of double porosity into consideration. Adopting this approach, Cai et al. (2018) established a hydro-mechanical coupled constitutive model based on the Glasgow Coupled Model that was validated against isotropic compression tests of double-porosity soils. Li et al. (2019) also used the effective degree of saturation to establish a model for unsaturated soils with double porosity. Their model used average effective stress, deviator stress and modified suction as the main stress variables. However, the model established by Cai et al (2018) is limited to isotropic loading and so cannot consider shear response. Also whilst the model established by Li et al. (2019) can consider shear response it adopts average effective stress as one of the main stress variables and so cannot consider how the three principal stresses will change respectively in a triaxial space, such as during shear at a constant net mean stress. A second way is to establish mutually independent models for the loading behaviour of macropores and micropores. For example, Mašin (2013) used different constitutive models for the behaviour of macropores and micropores and satisfactorily reproduced macro-mechanical properties by establishing a corresponding coupling relationship. However, this model has a complex form and requires determination of numerous material parameters, which limits its practical application.

This paper introduces a microstructurally based constitutive model for unsaturated

soils with double porosity. The key contribution is that the model adopts effective degree of saturation as the microstructural index and uses the Glasgow Coupled Model as the basic framework to acquire a concise constitutive relationship, which needs only nine physically meaningful parameters. The generalized tensor and Modified Camclay Model (Roscoe and Burland 1968) were adopted to extend the model to a three-dimensional space where both isotropic compression and shear loading can be simulated. The model is validated through experimental results of low-expansive Speswhite kaolin (Sivakumar 1993), low-plastic clay (Almahbobi 2018) and non-expansive Jossigny silt (Cui and Delage 1996) in terms of wetting, saturated and unsaturated, isotropic compression and shear tests.

CONSTITUTIVE MODEL

The effective degree of saturation was adopted to consider the effects of double porosity on the mechanical and hydraulic behaviour of unsaturated soils. The model was established based on the framework of the Glasgow Coupled Model (GCM) (Wheeler et al. 2003). The GCM is an important constitutive model which considers the impact of degree of saturation on effective stress and behaviour of unsaturated soils. Unlike other models which adopt a single loading-collapse yield curve in the net mean stress-suction plane to study the elasto-plastic mechanism during suction decrease or mechanical loading, the GCM utilises yield curves in the effective stress-modified suction plane (see **Fig. 1**). These yield curves are: the loading-collapse line (LC), which serves as the boundary between elastic volumetric change and plastic volumetric

86 change when the effective stress increases or decrease; the suction-decrease line (SD),
87 which acts as the boundary between elastic and plastic changes of degree of saturation
88 when suction decreases; and the suction-increase line (SI) which is defined to represent
89 the position where plastic change of degree of saturation will occur during suction
90 increase. According to Lloret-Cabot et al. (2013), the generalized stress tensor was
91 adopted to study both mechanical and hydraulic in a unified framework and Modified
92 Camclay Model (Roscoe and Burland 1968) was adopted to extend the model to a three-
93 dimensional space to study the shear behaviour of soils.

94 **Effective Degree of Saturation**

95 According to Alonso et al. (2010), pores within double-porosity soils can be
96 grouped into two categories: macropores partially filled with freely available water (the
97 main source of suction) and micropores filled with bound water. Correspondingly,
98 degree of saturation S_r can also be separated into two components: macroscopic degree
99 of saturation S_r^M, which contributes to the mechanical behaviour of soils, and
100 microscopic degree of saturation S_r^m, which is considered constant and independent of
101 applied suction and load ($S_r = S_r^m + S_r^M$). Subsequently the effective degree of
102 saturation can be defined as:

103 $$S_e = \frac{S_r - S_r^m}{1 - S_r^m} \quad (1)$$

104 with this definition, effective degree of saturation is a microstructurally based variable,
105 which considers the feature of double porosity and establishes a link between this

106 structure and the hydro-mechanical behaviour of soils. The effective degree of
107 saturation can be represented by the residual degree of saturation because it is related
108 to water stored within small occluded pores or intercrystalline pore space, where
109 physico-chemical bonds hold the water to the solid and are not strongly related to
110 applied suction or mechanical load, resulting in a very limited impact on effective stress
111 (Alonso et al. 2010).

112 **Stress Variables**

113 According to Houlsby's theory (Houlsby 1997), the increment of work input dW
114 per unit volume of unsaturated soil can be written as:

115 $$dW = [\sigma_{ij} - (S_r u_w + (1 - S_r) u_a \delta_{ij})] d\varepsilon_{ij} - (u_a - u_w) n dS_r \quad (2)$$

116 where σ_{ij} is the stress tensor, $d\varepsilon_{ij}$ is the strain increment tensor, δ_{ij} is the Kronecker
117 delta, u_w is the water pressure, u_a is the air pressure, S_r is the degree of saturation and
118 n is the porosity.

119 Incorporating the Bishop's effective stress (Bishop 1959) and the effective degree
120 of saturation S_e into (2), the expression of the Bishop's stress tensor σ_{ij}^* and the
121 modified suction s^* can be derived as:

122 $$\sigma_{ij}^* = \sigma_{ij} - (S_e u_w + (1 - S_e) u_a) \delta_{ij} \quad (3)$$

123 $$s^* = (u_a - u_w) n \quad (4)$$

124 Correspondingly, the stress and strain increment vectors have been adopted as
125 follows:

$$\mathbf{d\sigma}^{*} = (d\sigma_{xx}^{*}, d\sigma_{yy}^{*}, d\sigma_{zz}^{*}, d\sigma_{xy}^{*}, d\sigma_{yz}^{*}, d\sigma_{xz}^{*})^{T} \tag{5}$$

$$\mathbf{d\varepsilon} = (d\varepsilon_{xx}, d\varepsilon_{yy}, d\varepsilon_{zz}, d\varepsilon_{xy}, d\varepsilon_{yz}, d\varepsilon_{xz})^{T} \tag{6}$$

Following the approach of Lloret-Cabot et al. (2013) and taking the modified suction s^{*} and effective degree of saturation S_{e} as generalized stress and strain invariants, then the generalized stress and strain increment vectors can be written as:

$$\mathbf{d\sigma}^{*} = (d\sigma_{xx}^{*}, d\sigma_{yy}^{*}, d\sigma_{zz}^{*}, d\sigma_{xy}^{*}, d\sigma_{yz}^{*}, d\sigma_{xz}^{*}, ds^{*})^{T} \tag{7}$$

$$\mathbf{d\tilde{\varepsilon}} = (d\varepsilon_{xx}, d\varepsilon_{yy}, d\varepsilon_{zz}, d\varepsilon_{xy}, d\varepsilon_{yz}, d\varepsilon_{xz}, -dS_{\mathrm{e}})^{T} \tag{8}$$

For a hydro-mechanical coupled model, the increment of stress is the collective output of the force, suction and effective degree of saturation. According to (3) and (4), the formulas for the increments of generalized stress can be defined as:

$$d\sigma_{ij}^{*} = d(\sigma_{ij} - u_{\mathrm{a}}\delta_{ij}) + (sdS_{\mathrm{e}} + S_{\mathrm{e}}ds)\delta_{ij} \tag{9}$$

$$ds^{*} = nds - \frac{sd\varepsilon_{\mathrm{v}}}{v} \tag{10}$$

where $s = u_{\mathrm{a}} - u_{\mathrm{w}}$ is the suction, v is the specific volume and $d\varepsilon_{\mathrm{v}}$ is the increment of volumetric strain.

Yield Surfaces

Three yield surfaces, including the loading-collapse surface (LC), suction increase surface (SI) and suction decrease surface (SD) were adopted based on Lloret-Cabot et al., (2013), as seen in **Fig. 1**, in the q: p^{*}: s^{*} stress space (where q is the deviatoric stress, p^{*} is the mean Bishop's stress). The Modified CamClay Model (MCC), with a unique M (assuming that a unique Critical State Line in the q: p^{*} plane exists), was adopted as the reference model for the saturated condition. Then the algebraic expressions of the

three yield surfaces are given as follows:

$$F_{\mathrm{LC}} = q^2 - M^2 p^* (p_0^* - p^*) = 0 \tag{11}$$

$$F_{\mathrm{SI}} = s^* - s_{\mathrm{I}}^* = 0 \tag{12}$$

$$F_{\mathrm{SD}} = s_{\mathrm{D}}^* - s^* = 0 \tag{13}$$

where p_0^* is the Bishop's pre-consolidation pressure which defines the position of F_{LC}, s_{I}^* and s_{D}^* are the modified suctions that locate F_{SI} and F_{SD}, respectively.

Coupling between Yield Surfaces

Yielding on either of the three surfaces will lead to the movement of the other two surfaces. The plastic mechanisms and couplings of yield surfaces are defined as follows:

1) yielding on the LC yield surface (F_{SI}) will bring about plastic volumetric strain with no irreversible change of the effective degree of saturation S_{e}, which in turn triggers upward movements of the SI and SD surfaces. This coupling is established, with a coupling parameter k_2, by:

$$\frac{ds_{\mathrm{I}}^*}{s_{\mathrm{I}}^*} = \frac{ds_{\mathrm{D}}^*}{s_{\mathrm{D}}^*} = k_2 \frac{dp_0^*}{p_0^*} \tag{14}$$

2) yielding on the SI/SD yield surfaces ($F_{\mathrm{SI}} / F_{\mathrm{SD}}$) will lead to a plastic reduction of S_{e} but no change of plastic volumetric strain, which in turn induces upward/downward movement of the SD/SI surfaces and outward/inward movement of the LC surface. This coupling is established, with a coupling parameter k_1, by:

$$\frac{dp_0^*}{p_0^*} = k_1 \frac{ds_{\mathrm{I}}^*}{s_{\mathrm{I}}^*} = k_1 \frac{ds_{\mathrm{D}}^*}{s_{\mathrm{D}}^*} \tag{15}$$

166 **Flow Rules**

167 Flow rules define the orientation of the generalized plastic strain increments during
168 yielding. This paper assumes associated flow rules and adopts the generalized
169 expression presented by Lloret Cabot et al., (2013) :

170 $$d\tilde{\boldsymbol{\varepsilon}}_j^{\mathrm{p}} = d\lambda_l^j \frac{\partial F_l}{\partial \boldsymbol{\sigma}^*} \quad \text{with} \quad l = \mathrm{LC}, \beta;\ j = \mathrm{LC}, \beta, \mathrm{LC}+\beta;\ \beta = \mathrm{SI} \quad \text{or} \quad \mathrm{SD} \qquad (16)$$

171 where $d\lambda_l^j$ is the plastic multiplier with j related to the plastic mechanism which is
172 active (e.g. when yield on LC yield surface is activated j is LC and for yield on SI or
173 SD j is LC is β) and l is associated with plastic changes of effective degrees of
174 saturation (when l is β) or volumetric strains (when l is LC).

175 **Hardening Laws**

176 The generalized hardening laws determining the relationships between increments
177 of plastic volumetric strain $d\varepsilon_{\mathrm{v}}^{\mathrm{p}}$, increments of the plastic effective degree of saturation
178 $dS_{\mathrm{e}}^{\mathrm{p}}$, and increments of the hardening variables dp_o^*, ds_{I}^*, ds_{D}^* are as follows:

179 $$dp_o^* = p_0^* \left[\frac{v d\varepsilon_{\mathrm{v}}^{\mathrm{p}}}{\lambda - \kappa} - \frac{k_1 dS_{\mathrm{e}}^{\mathrm{p}}}{\lambda_{\mathrm{s}} - \kappa_{\mathrm{s}}} \right] \qquad (17)$$

180 $$ds_{\mathrm{I/D}}^* = s_{\mathrm{I/D}}^* \left[-\frac{dS_{\mathrm{e}}^{\mathrm{p}}}{\lambda_{\mathrm{s}} - \kappa_{\mathrm{s}}} + k_2 \frac{v d\varepsilon_{\mathrm{v}}^{\mathrm{p}}}{\lambda - \kappa} \right] \qquad (18)$$

181 **Generalized Stress-Strain Relationship**

182 Current knowledge on the elasto-plastic mechanisms of unsaturated soils indicates
183 that the generalized strains can be separated into elastic and plastic components (Lloret-

Cabot et al. 2013), so the increment of total generalized strains can be expressed as:

$$d\tilde{\boldsymbol{\varepsilon}} = d\tilde{\boldsymbol{\varepsilon}}^{\mathrm{e}} + d\tilde{\boldsymbol{\varepsilon}}_j^{\mathrm{p}} \quad \text{with} \quad j = \mathrm{LC}, \beta, \mathrm{LC}+\beta; \beta = \mathrm{SI} \quad \text{or} \quad \mathrm{SD} \tag{19}$$

where j is as defined in equation (16).

When only one elastic mechanism is activated, the generalized stress-strain relationship can be expressed as:

$$d\boldsymbol{\sigma}^{*} = \mathbf{D}_{\mathrm{e}}^{*} d\tilde{\boldsymbol{\varepsilon}}^{\mathrm{e}} \tag{20}$$

where $\mathbf{D}_{\mathrm{e}}^{*}$ is the generalized elastic matrix written in terms of the elastic bulk modulus K, the slope of the scanning curve in the water retention plane κ_{s} and the Poisson's ratio μ. Full details of $\mathbf{D}_{\mathrm{e}}^{*}$ and $\mathbf{D}_{\mathbf{ep}}^{*}$, the generalized elasto-plastic matrix, are presented in Appendix A.

There are nine parameters required in this microstructurally related constitutive model, namely λ, κ, k_1, k_2, M, μ, λ_{s}, κ_{s} and S_{res}. λ and κ are the slopes of normal consolidation line for saturated soil and slope of rebound curve, and they are related to the volumetric deformation during loading. k_1 and k_2 reflect the coupled movement between yield surfaces. To determine k_1 and k_2, two sets of data where both plastic volumetric strain and plastic change of degree of saturation are witnessed during loading (the parameters can be determined by using this data to solve equation (17) and equation (18)). M is a parameter that represents the relationship between deviator stress and effective stress under critical state and can be acquired by considering standard triaxial test data. μ is Poisson's ratio. λ_{s}、κ_{s} and S_{res} are the slopes of the main drying/wetting curve, the slope of scanning curve and residual degree of saturation,

205 respectively. The residual degree of saturation can be gained by drawing two tangents
206 at the start point and end point of the residual phase in a soil-water characteristic curve
207 and taking the degree of saturation at the intersection as the residual degree of saturation
208 (Eyo et al. 2022).

209 **MODEL VALIDATION**

210 To test the applicability of the proposed model, reported behaviour of a series of
211 statically compacted samples of soils with double porosity (Speswhite kaolin, low-
212 plastic clay and Jossigny silt) are considered. Speswhite kaolin is a low-expansive clay
213 with dominant mineral as kaolinite and 75% clay fraction, which has a higher rate of
214 consolidation compared with other clay soils (Sivakumar 1993). The low-plastic soil
215 is a mixture of 40% Leighton Buzzard sand, 40% M400 silt and 20% Speswhite kaolin
216 (Almahbobi, 2018). The soil showed significant collapsibility, in that it had a 16.2%
217 vertical strain in a single oedometer test where the specimens were compacted at water
218 content of 10% and dry unit weight of 14kN/m^3, and applied vertical pressure was
219 increased to 50kPa. The plasticity index is 8%. According to the Unified Soil
220 Classification System (USCS), the soil can be classified as low-plastic clay. Jossigny
221 silt originates from the eastern region of Paris and typically shows little swelling on
222 wetting. The soil is composed of illite, kaolinite and interstratified illite-smectite. The
223 liquid limit and plastic limit are 37% and 19%, respectively (Cui and Delage 1996).

224 Experimental data in terms of wetting, isotropic compression and shear response of
225 these soils are used to validate the model's performance.

Speswhite Kaolin

Isotropic compression

Suction-controlled triaxial tests reported by Sivakumar (1993) on compacted samples of Speswhite kaolin and conducted under both isotropic compression and shear have been considered. For isotropic loading, Path 1 was carried out by compressing the initial sample (mean net stress $\bar{p}$ =50kPa) to $\bar{p}$ =250kPa at a constant suction of 300kPa; Path 2 was carried out by wetting the initial sample (mean net stress $\bar{p}$ =50kPa) to s=100kPa and then compressing it to $\bar{p}$ =200kPa at a constant suction of 100kPa (see **Fig. 2**). Model parameters and initial states given by Lloret-Cabot et al. (2013) are shown in **Table 1**.

For both isotropic loading paths, the increasing net mean stress $\bar{p}$ resulted in overall compression and a decrease in void ratio. As noted by Lloret-Cabot et al. (2013), the initial stress state lay on the SD yield surface for both paths. This meant that as the modified suction reduced, yielding invariably occurred on the SD yield surface, which brought about a coupled inward movement of the LC yield surface and downward movement of SI yield surface. Before yielding on the SD surface there was no significant change in the void ratio or degree of saturation mainly because the modified suction did not decrease rapidly. In path 1, when the mean effective stress reached about 275kPa, the sample yielded on both the LC and SD yield surface. This yielding induced considerable amounts of plastic volumetric strain resulting in a significant decrease in void ratio (see **Fig. 3** (b)). Since the yielding on the LC yield surface results in a coupled

247 upward movement of the SD yield surface, this also generated a significant increase in
248 degree of saturation (see **Fig. 3** (c)). **Fig. 3** also presents a similar pattern of behaviour
249 for Path 2. Overall, it can also be seen that the proposed model is able to reproduce
250 well the isotropic loading behaviour of the Speswhite kaolin sample.

251 *Shear loading*

252 The loading of Speswhite kaolin samples included shear tests at constant confining
253 stress and constant mean net stress. Both tests were carried out while suction remained
254 unchanged. Before conducting the shear test at constant confining stress the sample was
255 compressed from initial conditions of $\bar{p}$=50kPa and s=300kPa to $\bar{p}$=150kPa. The
256 axial stress σ_1 was then increased until reaching failure (σ_2=σ_3=150kPa ,
257 $s = 300\text{kPa}$). For shear tests at constant net mean stress, the loading path included
258 wetting the initial sample ($\bar{p}$=50kPa and s=300kPa) to s=100kPa and then compressing
259 it to $\bar{p}$=200kPa before shearing it until failure. The model parameters and initial states
260 are again as presented in **Table 1**.

261 **Fig. 4** shows the simulated and experimental results of shear tests at constant
262 confining stress and net mean stress. The constant confining stress path yielded on both
263 the LC and SD yield surface due to the previous isotropic compression where the net
264 mean stress was increased to 150kPa. Yielding on the LC yield surface brought about
265 significant plastic volumetric deformation and a decrease of void ratio (see **Fig. 4** (b)).
266 Meanwhile, the coupled upward movement of the SD yield surface resulted in a
267 significant increase in degree of saturation (see **Fig. 4** (c)). As shown in **Fig. 4**, the

simulated stress path is consistent with the experimental path, however the developed axial strain ε_a is larger compared with the observed behaviour. This over prediction of axial strain whilst a soil tends towards critical state is a previously reported phenomenon which is attributed to the deficiency of the Modified Camclay Model (Lloret-Cabot et al. 2013). Generally, it can be observed that the proposed model can satisfactorily reproduce the development of void ratio and degree of saturation during shear.

For the shear test at constant net mean stress, the yielding also occurred on the LC and SD yield surfaces and generated a large amount of plastic change of void ratio and degree of saturation (see **Fig. 4** (e) and (f)). Although the proposed model overestimates the axial strain at critical state (see **Fig. 4** (d)), it can generally represent the mechanical and hydraulic behaviour of the Speswhite kaolin sample.

Low-Plastic Clay

The soil samples were prepared by adding quantities of distilled water to dry mixtures with a target initial water content of 10%. Then the soil-water mixtures were compacted in a mould until an axial pressure equivalent to 998kPa was reached. The final dry unit weight of the soil samples was 15kN/m^3. The measured initial void ratio, degree of saturation and suction were 0.732, 36.2% and 563kPa, respectively, and for the tests considered here the sample was first isotropically loaded under a confining stress of 20kPa. Model parameters and initial states are estimated from calibrating experimental data of wetting, isotropic compression and shear tests provided by

289 Almahbobi (2018). λ , κ , k_1 and k_2 are from isotropic compression tests. M is
290 attained from shear tests and μ is assumed to be 0.3. λ_s , κ_s and S_{res} are obtained from
291 the reported soil-water characteristic curve. Model parameters and initial states are
292 shown in **Table 2**.

293 *Wetting*

294 The sample was initially wetted to a suction equivalent to 500kPa (at constant
295 confining stress of 20kPa) and compressed to net mean stress equivalent to 100kPa (at
296 constant suction of 500kPa), the suction of the sample was then decreased in a stepwise
297 manner to 5kPa. Experimentally observed behaviour showed the void ratio
298 monotonically decreasing during wetting, along with a decrease in effective stress. This
299 behaviour is consistent with the highly collapsible nature of the soil (Almahbobi 2018).
300 Degree of saturation increased significantly with suction decrease and was close to
301 saturation at the final suction of 5kPa. The proposed model simulated yielding on both
302 the LC and SD yield surfaces throughout the wetting stress path (the initial stress state
303 was located at the corner intersection of both) leading to a prediction of a significant
304 decrease in void ratio and increase of degree of saturation. The modelled behaviour is
305 consistent with the experimental behaviour, with the model successfully reproducing
306 the collapsibility and saturation increase observed during wetting (see **Fig. 5**).

307 *Isotropic compression*

308 For saturated compression, the initial samples were wetted to saturation at a
309 confining stress of 20kPa and then compressed to target net mean stresses of 100, 250

and 400kPa, respectively.

Table 3 compares experimentally reported and proposed model calculated void ratio and water content at the end of compression. Both the void ratio and water content decreased during compression due to the volumetric compression and water discharge induced by the increasing net mean stress. The differences between model results and experimental results are small with relative differences always less than 10% and below 5% for some data. It can be seen that the model performs well when predicting the void ratio and water content in a saturated compression test (see **Table 3**).

For unsaturated compression, the initial samples were wetted to a suction equivalent to 300kPa at the confining stress of 20kPa and then compressed to target net mean stresses of 100, 250 and 400kPa. Experimental and model results are again shown in Table 3 and it can be seen that the model matches the experimental behaviour well (relative differences are around 1% for void ratio and less than 10% for degree of saturation), demonstrating the effectiveness of the model in reproducing hydro-mechanical behaviour in unsaturated compression (see **Table 3**).

Shear loading

After the compression stage described above each of the saturated and unsaturated samples were sheared at a constant confining stress equivalent to the net mean stress at the end of compression. The experimentally measured void ratio and water content at the start of the shear loading stage were used in the proposed model.

In the saturated shear tests the deviatoric stress was observed to increase with

increase in axial strain and reached a peak at an axial strain of 25%. The samples with higher confining stress had a higher peak of deviatoric stress. The peaks of deviatoric stress were 172, 436 and 660kPa, respectively, for the samples with confining stress equivalent to 100, 250 and 400kPa. The volumetric strain also increased and the sample with larger confining stress generated more significant volumetric deformation. In the model, the stress path remained yielding on both LC and SD yield surfaces and so volumetric strain developed further during shear. The modelled deviatoric stresses were consistent with the experimental results (see **Fig. 6**(a)). The model also performs well in terms of void ratios (see **Fig. 6** (b)). Similar conclusions can also be drawn from the unsaturated shear tests with the model demonstrating satisfactory performance (see **Fig. 6** (c), (d)). For **Fig. 6** (d), the model satisfactorily reproduced the change of void ratio when the confining stress is 400kPa. However, whilst the model correctly captures the overall trends of decreasing volume during shear, it overpredicts the magnitude of changes in void ratio when the confining stresses are 100kPa and 250kPa.

Jossigny Silt

Cui and Delage (Cui and Delage 1996) studied the yielding and plastic behaviour of unsaturated compacted samples of the Jossigny silt through isotropic compression and shear tests. According to the experimental results reported by Cui and Delage (1996), λ, κ, k_1 and k_2 are based on the isotropic compression tests. M is attained from shear tests and μ is assumed to be 0.3. λ_s and κ_s are obtained from the reported soil-water characteristic curve. The model parameters and initial states are presented in

352 **Table 4**. The microscopic degree of saturation S_{res} was estimated by Alonso et al
353 (2010).

354 The samples were firstly wetted to target suctions (200, 400, 800 and 1500kPa) and
355 then compressed to target net mean stresses (50, 100, 200, 400 and 600kPa) before they
356 were sheared at constant cell pressures (50, 100, 200, 400 and 600kPa). The shear stage
357 terminated when the critical state was reached.

358 *Isotropic compression*

359 **Table 5** presents the comparison between model results and experimental results
360 for isotropic compression at both a constant suction equivalent to 200kPa and at a
361 constant net mean stress equivalent to 200kPa. It can be concluded that the model
362 performs well in isotropic compression with the simulated development of void ratio
363 and degree of saturation satisfactorily consistent with the experimental results.

364 *Shear*

365 Shear tests were conducted after the target suctions and net mean stresses were
366 reached in the compression tests mentioned above. Shear tests continued until the
367 critical state was reached. **Fig. 7** presents the deviatoric stress/void ratio-axial strain
368 relationship in shear tests at constant suction equivalent to 200kPa and **Table 6** shows
369 the comparison on degree of saturation between model results and experimental results
370 when critical states are reached.

371 In general, the model can reproduce the changing trend of deviatoric stress with
372 respect to the axial strain despite the model tending to overestimate the axial strain at a

specific deviatoric stress (see **Fig. 7** (a)). The model also performs well in predicting the trends in degree of saturation (see **Table 6**) during shear but does overpredict the magnitude of the change of void ratio, as shown in **Fig. 7** (b). It is noted that as the wetting and compression steps, undertaken before shearing commenced, are also included in the simulation there is different in the predicted and measured void ratios at zero axial strain. It can also be noticed in **Fig. 7** (a) that there are discontinuities of the gradient for shear tests at cell pressure equivalent to 50 and 200kPa because the stress paths for these tests reached the LC yield surface during shearing. The stress path for the shear test at cell pressure equivalent to 600kPa had reached the LC yield surface during the isotropic compression stage so there is no discontinuity observed on the curve.

For shear tests at constant cell pressure equivalent to 200kPa, **Fig. 7** (c), (d) present the deviatoric stress/void ratio-axial strain relationship and **Table 6** shows the comparison on degree of saturation between model results and experimental results at the end of shear tests. It is clear that the model performs well under different suctions by satisfactorily reproducing the trends of behaviour but does exhibit a tendency to overpredict the magnitude of changes in void ratio.

CONCLUSIONS

A hydro-mechanical coupled constitutive model for unsaturated soils with double porosity is proposed in this paper, based on the framework of Glasgow Coupled Model. Since the Glasgow Coupled Model does not consider microstructure, the model

394 established in this paper adopts effective degree of saturation as a microstructural index
395 and introduces this index into Bishop's effective stress to establish the Bishop's
396 effective stress formula that can consider the characteristics of the double porosity. The
397 model also adopted the Modified Camclay Model in the average effective stress-
398 deviatoric stress plane. The expressions of the model were derived by combining the
399 generalized stress-strain tensor, associated flow law, hardening law and consistency
400 conditions. The novelty of the established model lies in the combination of effective
401 degree of saturation, Glasgow Coupled Model and Modified Camclay Model to provide
402 a convenient and straightforward way to model the behaviour of double-porosity soils
403 utilising only nine physically meaningful parameters.

404 The model has been validated against experimentally observed behaviour of
405 double-porosity samples, such as the compacted samples of Speswhite kaolin (low-
406 expansive), low-plastic clay (highly collapsible) and Jossigny silt (non-expansive). The
407 validation results show that the model is able to predict with reasonable accuracy the
408 hydro-mechanical coupled characteristics of unsaturated soils with double porosity,
409 whether the soil is collapsible or non-expansive. In terms of isotropic compression and
410 wetting behaviour, the model satisfactorily reproduces both the mechanical behaviour
411 (the variation of the modified suction and the void ratio) and hydraulic behaviour (the
412 variation of degree of saturation). The model also performs well in terms of shear
413 response. The model results are generally consistent with the experimental results in
414 terms of void ratio and degree of saturation, but the model, to some extent, overpredicts

415 the axial strain at specific deviatoric stress. This feature is not unexpected as the
416 Modified Camclay Model usually overestimates the axial strain developed during shear
417 on the path to reach critical state. Overall, it is demonstrated that the inclusion of
418 effective degree of saturation in such model is beneficial to consider the effect of
419 microstructure, especially double porosity, on the behaviour of unsaturated soils and
420 the proposed model is reliable in predicting the hydro-mechanical coupled behaviour
421 of collapsible and non-expansive soils with double porosity.

422

423 **APPENDIX A**

424 The full expression for $\mathbf{D}_{\mathrm{e}}^{*}$ is given as follows:

425
$$\mathbf{D}_{\mathrm{e}}^{*}=\begin{pmatrix} E_{11} & E_{12} & E_{13} & 0 & 0 & 0 & 0 \\ E_{21} & E_{22} & E_{23} & 0 & 0 & 0 & 0 \\ E_{31} & E_{32} & E_{33} & 0 & 0 & 0 & 0 \\ 0 & 0 & 0 & E_{44} & 0 & 0 & 0 \\ 0 & 0 & 0 & 0 & E_{55} & 0 & 0 \\ 0 & 0 & 0 & 0 & 0 & E_{66} & 0 \\ 0 & 0 & 0 & 0 & 0 & 0 & E_{77} \end{pmatrix}=\begin{pmatrix} \mathbf{D}_{\mathrm{e}\ 6\times6} & 0 \\ 0 & \gamma_{\mathrm{e}\ 1\times1} \end{pmatrix} \tag{21}$$

426
$$E_{11}=E_{22}=E_{33}=K+\frac{4}{3G}=\left(\frac{\nu}{\kappa}\right)p^{*}+\frac{4}{3G} \tag{22}$$

427
$$E_{44}=E_{55}=E_{66}=G=\frac{3K\left(1-2\mu\right)}{2\left(1+\mu\right)} \tag{23}$$

428
$$E_{12}=E_{23}=E_{13}=K-\frac{2}{3G} \tag{24}$$

429
$$E_{77}=\gamma_{\mathrm{e}}=\left(\frac{1}{\kappa_{\mathrm{s}}}\right)s^{*} \tag{25}$$

430 where K is the bulk modulus and G is the shear modulus.

431 When a plastic mechanism is active, the generalized stress-strain relationship can

be also assumed as follows:

$$d\boldsymbol{\sigma}^{*} = \mathbf{D}_{\mathrm{e}}^{*} d\tilde{\boldsymbol{\varepsilon}}^{\mathrm{e}} = \mathbf{D}_{\mathbf{ep}}^{*} d\tilde{\boldsymbol{\varepsilon}} \tag{26}$$

$\mathbf{D}_{\mathbf{ep}}^{*}$ is the generalized elasto-plastic matrix, depending on the specific plastic mechanism(s) active during loading. $\mathbf{D}_{\mathbf{ep}}^{*}$ is unknown hitherto, but the expression of it can be obtained by the following approach.

Considering the general case that two plastic mechanisms are active, the expression (26) can be written as

$$d\boldsymbol{\sigma}^{*} = \mathbf{D}_{\mathbf{e}}^{*} d\tilde{\boldsymbol{\varepsilon}}^{\mathbf{e}} = \mathbf{D}_{\mathbf{e}}^{*}\left(d\tilde{\boldsymbol{\varepsilon}} - d\tilde{\boldsymbol{\varepsilon}}_{\mathrm{LC}+\beta}^{\mathrm{p}}\right) \tag{27}$$

Then considering the flow rule (16),

$$d\tilde{\boldsymbol{\varepsilon}}_{\mathrm{LC}+\beta}^{\mathrm{p}} = d\lambda_{\mathrm{LC}}^{\mathrm{LC}+\beta} \frac{\partial F_{\mathrm{LC}}}{\partial \boldsymbol{\sigma}^{*}} + d\lambda_{\beta}^{\mathrm{LC}+\beta} \frac{\partial F_{\beta}}{\partial \boldsymbol{\sigma}^{*}} \tag{28}$$

To keep the end of the stress path invariably attached on yield surfaces after yielding, the consistency condition on F_{LC} and F_{β} should be considered:

$$dF_{\mathrm{LC}} = \left(\frac{\partial F_{\mathrm{LC}}}{\partial \boldsymbol{\sigma}^{*}}\right)^{T} d\boldsymbol{\sigma}^{*} + \frac{\partial F_{\mathrm{LC}}}{\partial p_{0}^{*}} dp_{0}^{*} = 0 \tag{29}$$

$$dF_{\beta} = \left(\frac{\partial F_{\beta}}{\partial s^{*}}\right)^{T} ds^{*} + \frac{\partial F_{\beta}}{\partial s_{\beta}^{*}} ds_{\beta}^{*} = 0 \tag{30}$$

Incorporating (29), (30) and hardening laws (17) and (18), the following expressions can be obtained:

$$\left(\frac{\partial F_{\beta}}{\partial s^{*}}\right)^{T} (-\gamma_{\mathrm{e}})\left(dS_{\mathrm{e}} - d\lambda_{\beta}^{\mathrm{LC}+\beta} \frac{\partial F_{\beta}}{\partial s^{*}}\right) + \frac{\partial F_{\beta}}{\partial s_{\beta}^{*}} s_{\beta}^{*}\left[-\frac{d\lambda_{\beta}^{\mathrm{LC}+\beta} \dfrac{\partial F_{\beta}}{\partial s^{*}}}{\lambda_{\mathrm{s}} - \kappa_{\mathrm{s}}} + k_{2} \frac{\nu m^{T} d\lambda_{\mathrm{LC}}^{\mathrm{LC}+\beta} \dfrac{\partial F_{\mathrm{LC}}}{\partial \boldsymbol{\sigma}^{*}}}{\lambda - \kappa}\right] = 0 \tag{31}$$

$$\left(\frac{\partial F_{\mathrm{LC}}}{\partial \boldsymbol{\sigma}^{*}}\right)^{T}\mathbf{D}_{\mathrm{e}}\left(d\boldsymbol{\varepsilon}-d\chi_{\mathrm{LC}}^{\mathrm{LC}+\beta}\frac{\partial F_{\mathrm{LC}}}{\partial \boldsymbol{\sigma}^{*}}\right)+\frac{\partial F_{\mathrm{LC}}}{\partial p_{o}^{*}}\,p_{o}^{*}\left[v\frac{m^{T}d\lambda_{\mathrm{LC}}^{\mathrm{LC}+\beta}\frac{\partial F_{\mathrm{LC}}}{\partial \boldsymbol{\sigma}^{*}}}{\lambda-\kappa}-\frac{k_{1}d\lambda_{\beta}^{\mathrm{LC}+\beta}\frac{\partial F_{\beta}}{\partial s^{*}}}{\lambda_{\mathrm{s}}-\kappa_{\mathrm{s}}}\right]=0 \quad (32)$$

Then the plastic multiplies can be derived as:

$$d\lambda_{\mathrm{LC}}^{\mathrm{LC}+\beta}=\frac{\mathbf{a}_{\mathrm{LC}+\beta}^{T}d\boldsymbol{\varepsilon}+b_{\mathrm{LC}+\beta}dS_{\mathrm{e}}}{h_{\mathrm{LC}+\beta}} \quad (33)$$

$$d\lambda_{\beta}^{\mathrm{LC}+\beta}=\frac{\mathbf{c}_{\mathrm{LC}+\beta}^{T}d\boldsymbol{\varepsilon}+d_{\mathrm{LC}+\beta}dS_{\mathrm{e}}}{h_{\mathrm{LC}+\beta}} \quad (34)$$

where

$$\mathbf{a}_{\mathrm{LC}+\beta}^{T}=\left(\frac{\partial F_{\mathrm{LC}}}{\partial \boldsymbol{\sigma}^{*}}\right)^{T}\mathbf{D}_{\mathbf{e}}\left(\frac{\partial F_{\beta}}{\partial s^{*}}\gamma_{\mathrm{e}}\frac{\partial F_{\beta}}{\partial s^{*}}-\frac{\partial F_{\beta}}{\partial s_{\beta}^{*}}s_{\beta}^{*}\frac{1}{\lambda_{\mathrm{s}}-\kappa_{\mathrm{s}}}\frac{\partial F_{\beta}}{\partial s^{*}}\right) \quad (35)$$

$$b_{\mathrm{LC}+\beta}=-k_{1}\frac{\partial F_{\beta}}{\partial s^{*}}\gamma_{e}\frac{\partial F_{\mathrm{LC}}}{\partial p_{0}^{*}}\frac{p_{0}^{*}}{\lambda_{\mathrm{s}}-\kappa_{\mathrm{s}}}\frac{\partial F_{\beta}}{\partial s^{*}} \quad (36)$$

$$\mathbf{c}_{\mathrm{LC}+\beta}^{T}=k_{2}\left(\frac{\partial F_{\mathrm{LC}}}{\partial \boldsymbol{\sigma}^{*}}\right)^{T}\mathbf{D}_{\mathbf{e}}\frac{\partial F_{\beta}}{\partial s_{\beta}^{*}}v\frac{s_{\beta}^{*}}{\lambda-\kappa}m^{T}\frac{\partial F_{\mathrm{LC}}}{\partial \boldsymbol{\sigma}^{*}} \quad (37)$$

$$d_{\mathrm{LC}+\beta}=\frac{\partial F_{\beta}}{\partial s^{*}}\gamma_{\mathrm{e}}\left(-\left(\frac{\partial F_{\mathrm{LC}}}{\partial \boldsymbol{\sigma}^{*}}\right)^{T}\mathbf{D}_{\mathbf{e}}\frac{\partial F_{\mathrm{LC}}}{\partial \boldsymbol{\sigma}^{*}}+\frac{\partial F_{\mathrm{LC}}}{\partial p_{0}^{*}}\frac{v}{\lambda-\kappa}m^{T}\frac{\partial F_{\mathrm{LC}}}{\partial \boldsymbol{\sigma}^{*}}\right) \quad (38)$$

$$\begin{aligned}h_{\mathrm{LC}+\beta}=&\left[-\left(\frac{\partial F_{\mathrm{LC}}}{\partial \boldsymbol{\sigma}^{*}}\right)^{T}\mathbf{D}_{\mathbf{e}}\frac{\partial F_{\mathrm{LC}}}{\partial \boldsymbol{\sigma}^{*}}+\frac{\partial F_{\mathrm{LC}}}{\partial p_{0}^{*}}\frac{v}{\lambda-\kappa}p_{0}^{*}m^{T}\frac{\partial F_{\mathrm{LC}}}{\partial \boldsymbol{\sigma}^{*}}\right]\\&*\left[-\frac{\partial F_{\beta}}{\partial s^{*}}\gamma_{\mathrm{e}}\frac{\partial F_{\beta}}{\partial s^{*}}+\frac{\partial F_{\beta}}{\partial s_{\beta}^{*}}s_{\beta}^{*}\frac{1}{\lambda_{\mathrm{s}}-\kappa_{\mathrm{s}}}\frac{\partial F_{\beta}}{\partial s^{*}}\right]\\&-k_{1}k_{2}\frac{\partial F_{\beta}}{\partial s_{\beta}^{*}}p_{0}^{*}\frac{v}{\lambda-\kappa}s_{\beta}^{*}\frac{1}{\lambda_{\mathrm{s}}-\kappa_{\mathrm{s}}}\frac{\partial F_{\mathrm{LC}}}{\partial p_{0}^{*}}m^{T}\frac{\partial F_{\mathrm{LC}}}{\partial \boldsymbol{\sigma}^{*}}\frac{\partial F_{\beta}}{\partial s^{*}}\end{aligned} \quad (39)$$

Substituting these two plastic multipliers (33) and (34) into (26) and after some algebra, the generalized elasto-plastic matrix can be obtained as follows:

$$\mathbf{D}_{\mathbf{ep}}^{*}=\begin{pmatrix}\mathbf{A}_{\mathbf{LC}+\beta} & \mathbf{B}_{\mathbf{LC}+\beta}\\ \left(\mathbf{C}_{\mathbf{LC}+\beta}\right)^{T} & D_{\mathrm{LC}+\beta}\end{pmatrix} \quad (40)$$

where

$$\mathbf{A}_{\mathbf{LC}+\beta} = \mathbf{D}_{\mathbf{e}}\left(\mathbf{I}_{6\times 6} - \frac{\mathbf{a}^{T}_{\mathrm{LC}+\beta}}{h_{\mathrm{LC}+\beta}}\frac{\partial F_{\mathrm{LC}}}{\partial \boldsymbol{\sigma}^{*}}\right) \tag{41}$$

$$\mathbf{B}_{\mathbf{LC}+\beta} = \mathbf{D}_{\mathbf{e}}\left(\frac{\partial F_{\mathrm{LC}}}{\partial \boldsymbol{\sigma}^{*}}\frac{b_{\mathrm{LC}+\beta}}{h_{\mathrm{LC}+\beta}}\right) \tag{42}$$

$$\left(\mathbf{C}_{\mathbf{LC}+\beta}\right)^{T} = -\gamma_{\mathrm{e}}\left(\frac{\partial F_{\beta}}{\partial s^{*}}\frac{\mathbf{c}^{T}{}_{\mathrm{LC}+\beta}}{h_{\mathrm{LC}+\beta}}\right) \tag{43}$$

$$D_{\mathrm{LC}+\beta} = \gamma_{\mathrm{e}}\left(1+\frac{\partial F_{\beta}}{\partial s^{*}}\frac{d_{\mathrm{LC}+\beta}}{h_{\mathrm{LC}+\beta}}\right) \tag{44}$$

DATA AVAILABILITY STATEMENT

All data, models, or code that support the findings of this study are available from the corresponding author upon reasonable request.

ACKNOWLEDGEMENTS

This research was financially supported by the National Natural Science Foundation of China (U2034204, 52078031, U1834206), the Natural Science Foundation of Beijing Municipality (8202038), Fundamental Research Funds for the Central Universities (2021CZ109, 2021JBZ111), and the China Scholarship Council (CSC) from the Ministry of Education of P.R. China (CSC202007090010)

REFERENCES

Alazaiza, M. Y. D., Ngien, S. K., Bob, M. M., Kamaruddin, S. A., and Ishak, W. M. F.2017. “Influence of Macro-pores on DNAPL Migration in Double-Porosity Soil Using Light Transmission Visualization Method.” *Transp. Porous Media*, 117(1), 103–123. https://doi.org/10.1007/s11242-017-0822-3.

485 Almahbobi, S. A.2018. “Experimental study of volume change and shear strength
486 behaviour of statically compacted collapsible soil.” Cardiff University, UK.
487 Alonso, E. E., Pereira, J.-M., Vaunat, J., and Olivella, S.2010. “A microstructurally
488 based effective stress for unsaturated soils.” *Géotechnique*, 60(12), 913–925.
489 https://doi.org/10.1680/geot.8.P.002.
490 Bagherieh, A. R., Khalili, N., Habibagahi, G., and Ghahramani, A.2009. “Drying
491 response and effective stress in a double porosity aggregated soil.” *Eng. Geol.*,
492 105(1), 44–50. https://doi.org/10.1016/j.enggeo.2008.12.009.
493 Bishop, A. W.1959. “The Principle of Effective Stress.” *Tek. Ukebl.*, 39, 859–863.
494 Cai, G., He, X., Dong, L., Liu, S., and Sheng, D.2020a. “The shear and tensile strength
495 of unsaturated soils by a grain-scale investigation.” *Granul. Matter*, 22(1)
496 https://doi.org/10.1007/s10035-019-0969-4.
497 Cai, G. Q., Wang, Y. N., Zhou, A. N., and Zhao, C. G.2018. “A microstructure-
498 dependent hydro-mechanical coupled constitutive model for unsaturated soils.”
499 *Chin. J. Geotech. Eng.*, 40(04), 618–624.
500 https://doi.org/10.11779/CJGE201804005.
501 Cai, G., Zhou, A., Liu, Y., Xu, R., and Zhao, C.2020b. “Soil water retention behavior
502 and microstructure evolution of lateritic soil in the suction range of 0–
503 286.7MPa.” *Acta Geotech.*, 15, 3327–3341. https://doi.org/10.1007/s11440-
504 020-01011-w.
505 Cai, G., Zhou, A., and Sheng, D.2014. “Permeability function for unsaturated soils with

different initial densities." *Can. Geotech. J.*, 51(12), 1456–1467. https://doi.org/10.1139/cgj-2013-0410.

Casini, F., Vaunat, J., Romero, E., and Desideri, A.2012. "Consequences on water retention properties of double-porosity features in a compacted silt." *Acta Geotech.*, 7(2), 139–150. https://doi.org/10.1007/s11440-012-0159-6.

Cui, Y. J., and Delage, P.1996. "Yielding and plastic behaviour of an unsaturated compacted silt." *Géotechnique*, 46(2), 291–311. https://doi.org/10.1680/geot.1996.46.2.291.

Cuisinier, O., Auriol, J.-C., Le Borgne, T., and Deneele, D.2011. "Microstructure and hydraulic conductivity of a compacted lime-treated soil." *Eng. Geol.*, 123(3), 187–193. https://doi.org/10.1016/j.enggeo.2011.07.010.

Eyo, E. U., Ng'ambi, S., and Abbey, S. J.2022. "An overview of soil–water characteristic curves of stabilised soils and their influential factors." *J. King Saud Univ. - Eng. Sci.*, 34(1), 31–45. https://doi.org/10.1016/j.jksues.2020.07.013.

Houlsby, G. T.1997. "The work input to an unsaturated granular material." *Geotechnique*, 47(1), 193–196. https://doi.org/10.1680/geot.1997.47.1.193.

Jia, R., Lei, H., and Li, K.2020. "Compressibility and Microstructure Evolution of Different Reconstituted Clays during 1D Compression." *Int. J. Geomech.*, 20(10), 04020181. https://doi.org/10.1061/(ASCE)GM.1943-5622.0001830.

Lewandowska, J., Szymkiewicz, A., Burzyński, K., and Vauclin, M.2004. "Modeling

of unsaturated water flow in double-porosity soils by the homogenization approach." *Adv. Water Resour.*, 27(3), 283–296. https://doi.org/10.1016/j.advwatres.2003.12.004.

Li, J., Yin, Z.-Y., Cui, Y.-J., Liu, K., and Yin, J.-H.2019. "An elasto-plastic model of unsaturated soil with an explicit degree of saturation-dependent CSL." *Eng. Geol.*, 260, 105240. https://doi.org/10.1016/j.enggeo.2019.105240.

Li, J., Zhao, C., Cai, G., Asreazad, S., Xu, X. F., and Huang, Q.2013. "The input work expression and the thermodynamics-based modelling framework for unsaturated expansive soils with double porosity." *Chin. Sci. Bull.*, 58(27), 3422–3429. https://doi.org/10.1007/s11434-013-5828-9.

Lloret-Cabot, M., Sánchez, M., and Wheeler, S. J.2013. "Formulation of a three-dimensional constitutive model for unsaturated soils incorporating mechanical-water retention couplings: A 3D COUPLED CONSTITUTIVE MODEL FOR UNSATURATED SOILS." *Int. J. Numer. Anal. Methods Geomech.*, 37(17), 3008–3035. https://doi.org/10.1002/nag.2176.

Low, H.-E., Phoon, K.-K., Tan, T.-S., and Leroueil, S.2008. "Effect of soil microstructure on the compressibility of natural Singapore marine clay." *Can. Geotech. J.*, 45(2), 161–176. https://doi.org/10.1139/T07-075.

Manahiloh, K. N., Muhunthan, B., and Likos, W. J.2016. "Microstructure-based effective stress formulation for unsaturated granular soils." *Int. J. Geomech.*, 16(6), D4016006. https://doi.org/10.1061/(ASCE)GM.1943-5622.0000617.

548 Mašín, D.2013. “Double structure hydromechanical coupling formalism and a model
549 for unsaturated expansive clays.” *Eng. Geol.*, 165, 73–88.
550 https://doi.org/10.1016/j.enggeo.2013.05.026.
551 Mašín, D., Herbstová, V., and Boháč, J.2005. “Properties of double porosity clayfills
552 and suitable constitutive models.” *Proc. 16th Int. Conf. Soil Mech. Geotech.*
553 *Eng.*, IOS Press, 827–830. https://doi.org/10.3233/978-1-61499-656-9-827.
554 Musso, G., Romero, E., and Della Vecchia, G.2014. “Double-structure effects on the
555 chemo-hydro-mechanical behaviour of a compacted active clay.” *Bio- Chemo-*
556 *Mech. Process. Geotech. Eng.*, Conference Proceedings, ICE Publishing, 3–17
557 https://doi.org/10.1680/bcmpge.60531.001.
558 Ngien, S. K., Rahman, N. A., Ahmad, K., Rol, and Lewis, W.2012. “A review of
559 experimental studies on double-porosity soils.” *Sci. Res. Essays*, Academic
560 Journals, 7(38), 3243–3250. https://doi.org/10.5897/SRE11.2131.
561 Ranaivomanana, H., Razakamanantsoa, A., and Amiri, O.2017. “Permeability
562 prediction of soils including degree of compaction and microstructure.” *Int. J.*
563 *Geomech.*, 17(4), 04016107. https://doi.org/10.1061/(ASCE)GM.1943-
564 5622.0000792.
565 Romero, E., and Simms, P. H.2008. “Microstructure investigation in unsaturated soils:
566 a review with special attention to contribution of mercury intrusion porosimetry
567 and environmental scanning electron microscopy.” *Geotech. Geol. Eng.*, 26(6),
568 705–727. https://doi.org/10.1007/s10706-008-9204-5.

569 Roscoe, K., and Burland, J. B.1968. “On the generalized stress-strain behaviour of wet
570 clay.” *Eng. Plast.*, 535–609.
571 Russell, A. R.2010. “Water retention characteristics of soils with double porosity.” *Eur.*
572 *J. Soil Sci.*, 61(3), 412–424. https://doi.org/10.1111/j.1365-2389.2010.01237.x.
573 Sánchez, M., Gens, A., Villar, M. V., and Olivella, S.2016. “Fully coupled thermo-
574 hydro-mechanical double-porosity formulation for unsaturated soils.” *Int. J.*
575 *Geomech.*, 16(6), D4016015. https://doi.org/10.1061/(ASCE)GM.1943-
576 5622.0000728.
577 Sergeyev, Y. M., Grabowska-Olszewska, B., Osipov, V. I., Sokolov, V. N., and
578 Kolomenski, Y. N.1980. “The classification of microstructures of clay soils.” *J.*
579 *Microsc.*, 120(3), 237–260. https://doi.org/10.1111/j.1365-
580 2818.1980.tb04146.x.
581 Sivakumar, V.1993. “A critical state framework for unsaturated soil.” University of
582 Sheffield, United Kingdom.
583 Tian-er, M. A. O., and Lin, X. I. A.2010. “Experimental research on microstructure of
584 expansive soil in north of Hubei province.” *J. Huazhong Univ. Sci. Technol.*
585 *Urban Sci. Ed.*, 2 https://en.cnki.com.cn/Article_en/CJFDTotal-
586 WHCJ201002012.htm.
587 Trzciński, J., and Wójcik, E.2019. “Application of microstructure classification for the
588 assessment of the variability of geological-engineering and pore space
589 properties in clay soils.” *Open Geosci.*, 11(1), 236–248.

https://doi.org/10.1515/geo-2019-0019.

Wheeler, S. J., Sharma, R. S., and Buisson, M. S. R.2003. “Coupling of hydraulic hysteresis and stress–strain behaviour in unsaturated soils.” 53(1), 41–54. https://doi.org/10.1680/geot.2003.53.1.41.

Table 1. Model parameters and initial states for Speswhite kaolin (Lloret-Cabot et al. 2013)

Parameters		Initial states	
λ	0.124	$\overline{p}$ / kPa	50.00
κ	0.006	s / kPa	300.00
λ_s	0.098	e	1.208
κ_s	0.0076	S_r	60.1%
k_1	0.662	S_r^m	5.0%
k_2	0.803	p_0^* / kPa	273.00
M	0.71	S_D^* / kPa	164.00
μ	0.3	S_I^* / kPa	/

Table 2. Model parameters and initial states for the mixture

Parameters		Initial states	
λ	0.07	$\overline{p}$ / kPa	20.00
κ	0.008	s / kPa	563.00
λ_s	0.12	e	0.732
κ_s	0.02	S_r	36.2%
k_1	0.6	S_r^m	10.0%
k_2	0.3	p_0^* / kPa	250.00
M	1.076	S_D^* / kPa	237.94
μ	0.3	S_I^* / kPa	/

601 **Table 3.** Void ratios and water contents/degrees of saturation at the end of saturated

602 and unsaturated compression

	P_{net} (kPa)	e (model)	e (experiment)	w (model)	w (experiment)
	100	0.579	0.529	21.87%	19.90%
Saturated	250	0.490	0.476	18.49%	17.90%
	400	0.439	0.438	16.58%	16.50%
				S_r (model)	S_r (experiment)
	100	0.713	0.702	43.8%	40.7%
Unsaturated	250	0.665	0.661	46.2%	42.2%
	400	0.632	0.626	47.8%	43.6%

603 **Table 4.** Model parameters and initial states for the Jossigny silt samples

Parameters		Initial states	
λ	0.091	$\overline{p}$ / kPa	25.00
κ	0.013	s / kPa	200.00
λ_s	0.131	e	0.629
κ_s	0.008	S_r	76.4%
k_1	0.65	S_r^m	56.0%
k_2	0.66	p_0^* / kPa	374.60
M	1.02	S_D^* / kPa	77.23
μ	0.3	S_I^* / kPa	103.84

604 **Table 5.** Results for the compression at constant suction/net mean stress

s (kPa)	p_{net} (kPa)	e (model)	e (experiment)	S_r (model)	S_r (experiment)
200	600	0.502	0.569	82.0%	84.0%
200	200	0.617	0.599	76.5%	77.0%
200	50	0.626	0.621	76.4%	77.0%
400	200	0.545	0.577	75.1%	74.0%
800	200	0.570	0.599	70.1%	70.0%

605 **Table 6.** Results of degree of saturation in the critical state

s /kPa	σ_3 /kPa	S_r (model)	S_r (experiment)
200	600	94.3%	98.0%
200	200	85.7%	79.0%
200	50	79.2%	79.0%
400	200	76.3%	77.0%
800	200	70.1%	70.0%

606

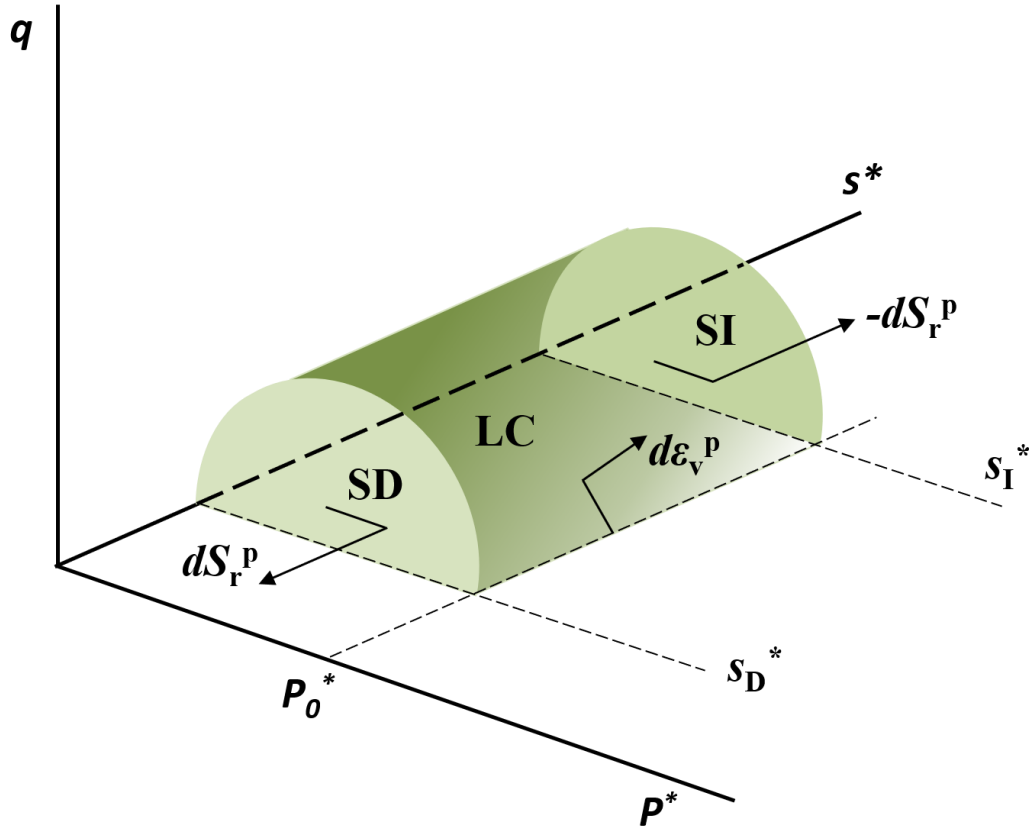

607

608 **Fig. 1.** Yield surfaces of the 3D generalized model (after Lloret-Cabot et al., 2013)

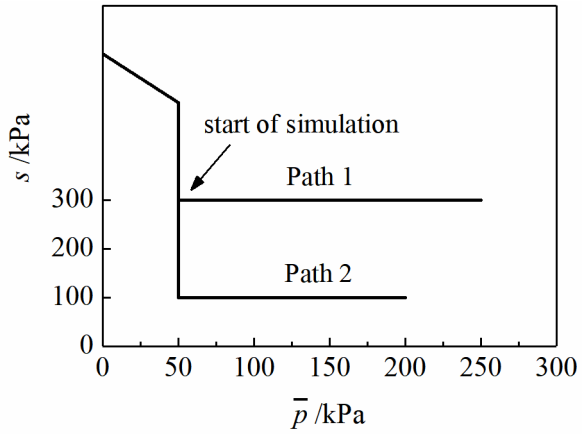

609

610 **Fig. 2.** Isotropic loading paths conducted by Sivakumar (Sivakumar, 1993)

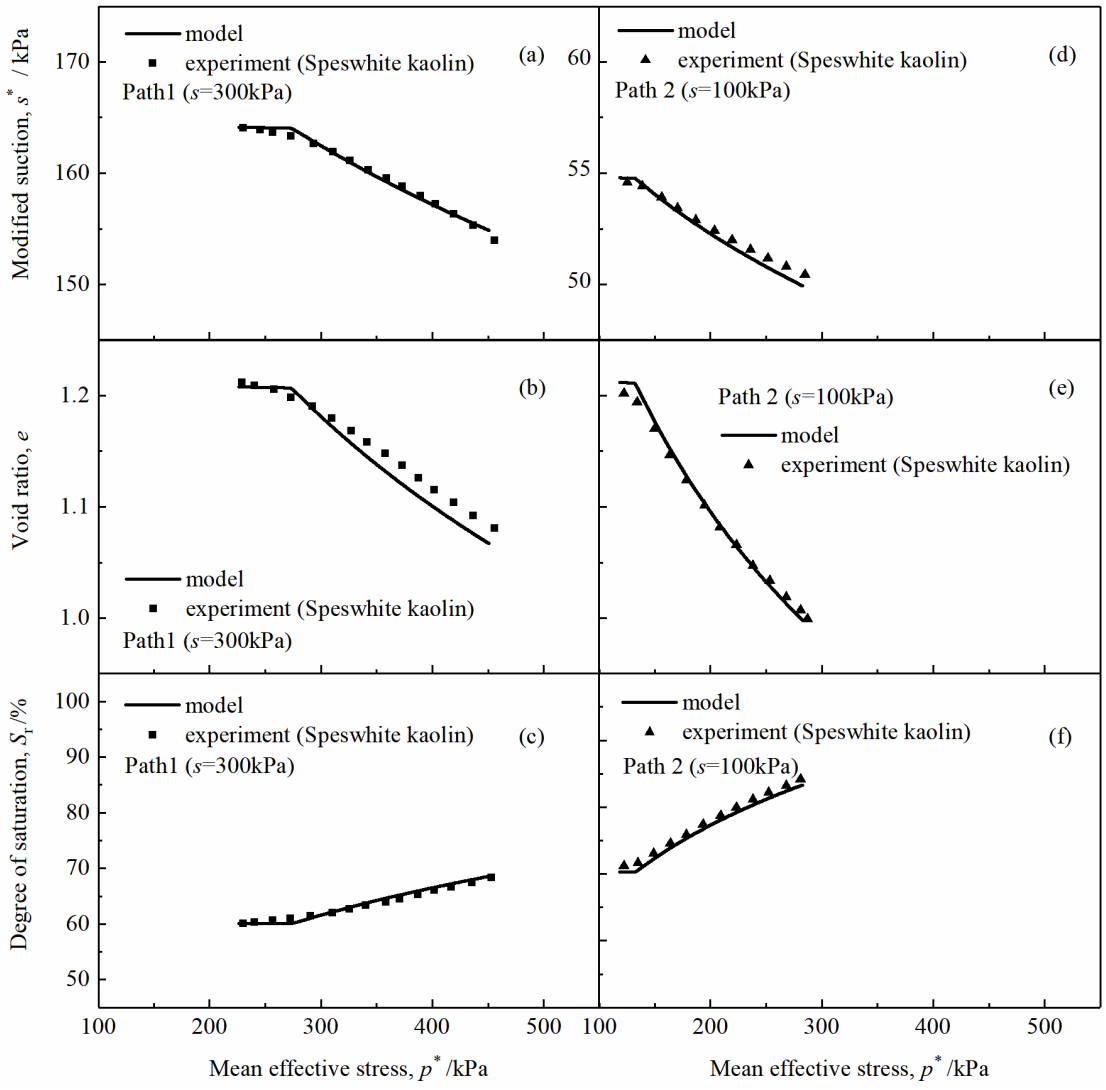

611

612 **Fig. 3.** Comparison between model results and experimental results on Speswhite

613 kaolin (Sivakumar, 1993) for Path 1and Path 2: (a/d) $p^* - s^*$; (b/e) $p^* - e$; (c/f)

614 $p^* - S_r$

615

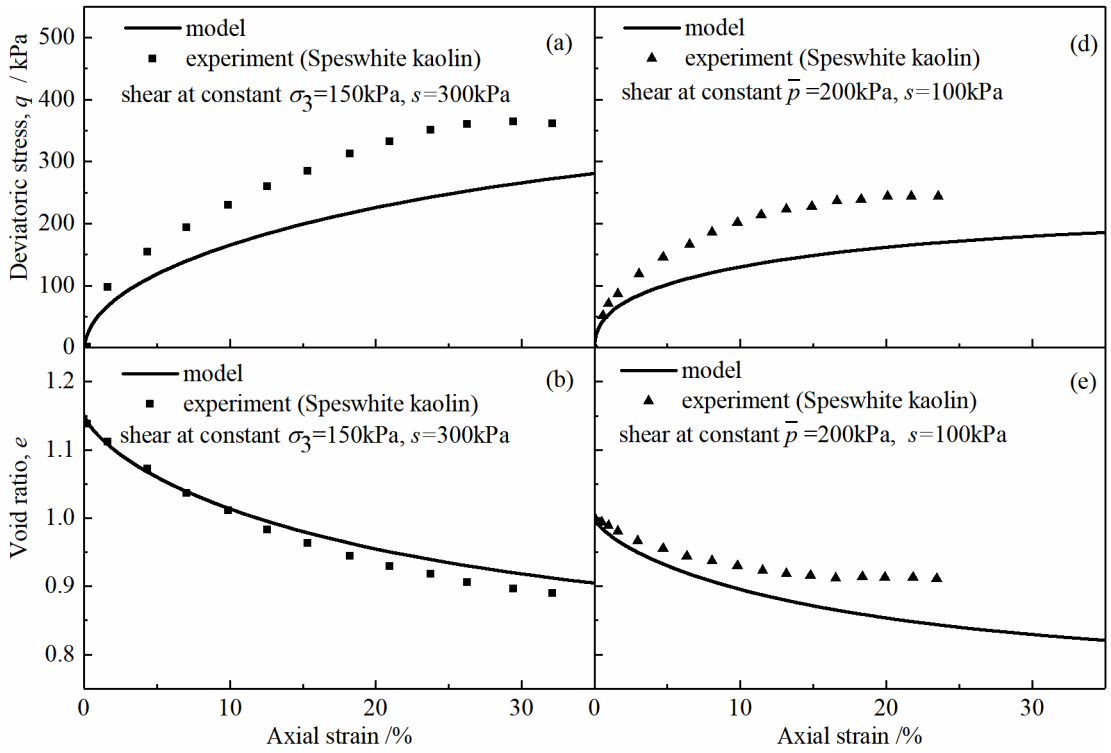

616

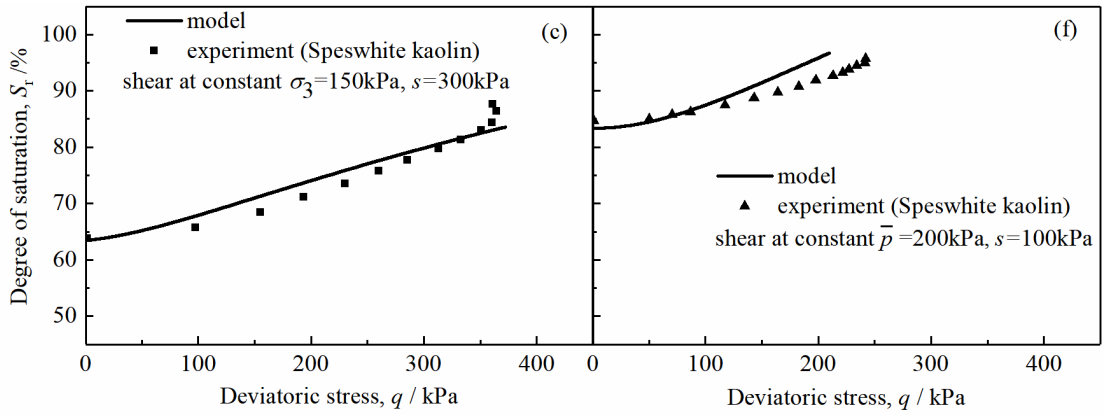

617 **Fig. 4.** Comparison between model results and experimental results (Sivakumar 1993)

618 for shear at constant confining stress and net mean stress: (a/d) $\varepsilon_a - q$; (b/e) $\varepsilon_a - e$;

619 (c/f) $q - S_r$

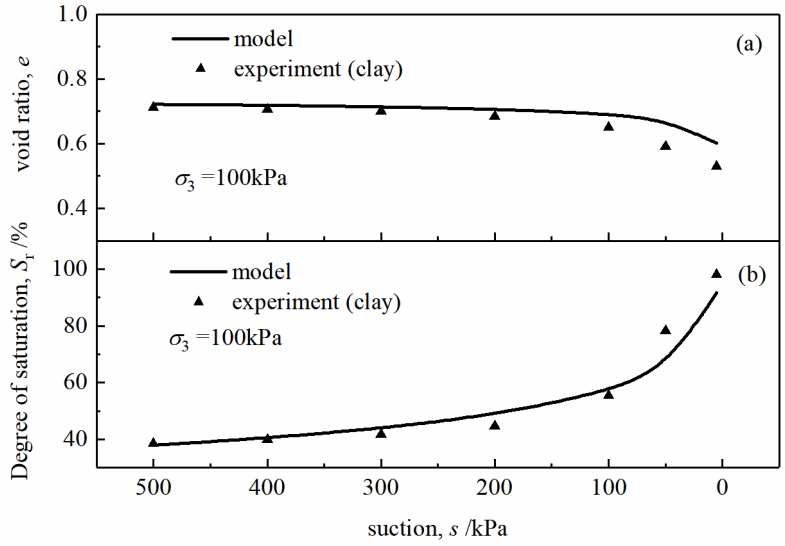

620

621 **Fig. 5**. Comparison between model results and experimental results on low-plastic

622 clay: (a) $s-e$; (b) $s-S_r$

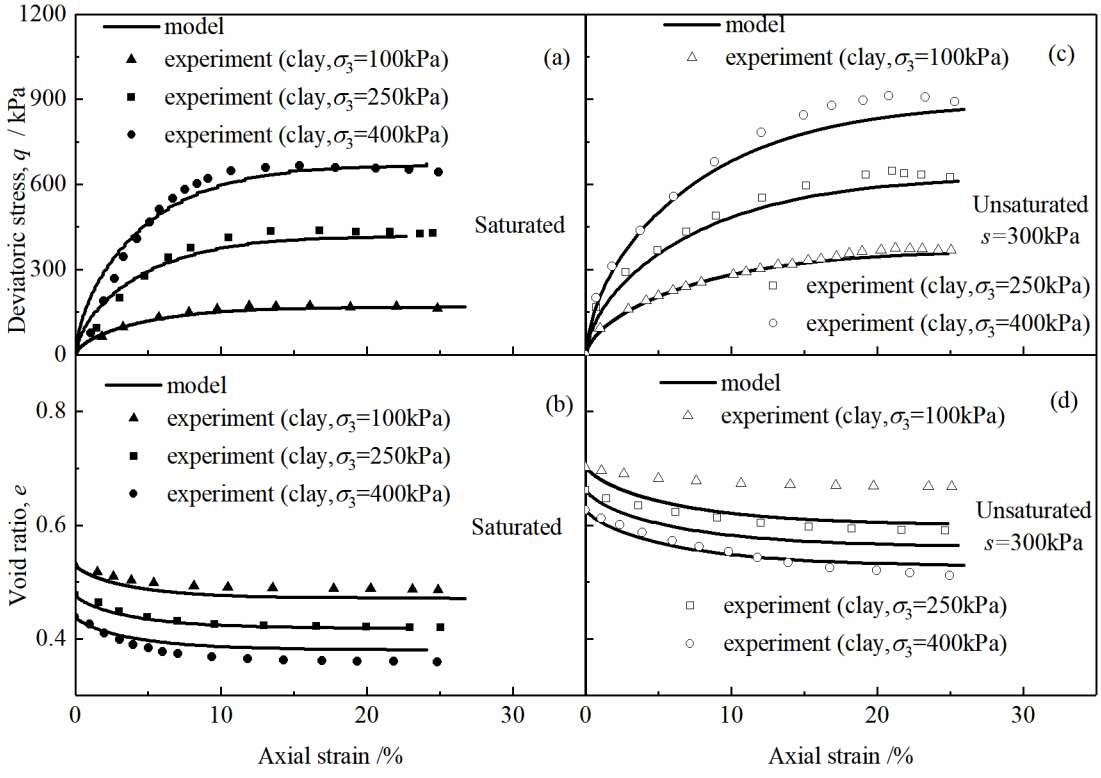

623

624 **Fig. 6**. Comparison between model results and experimental results (Almahbobi

625 2018) for saturated and unsaturated shear: (a/c) q; (b/d) e

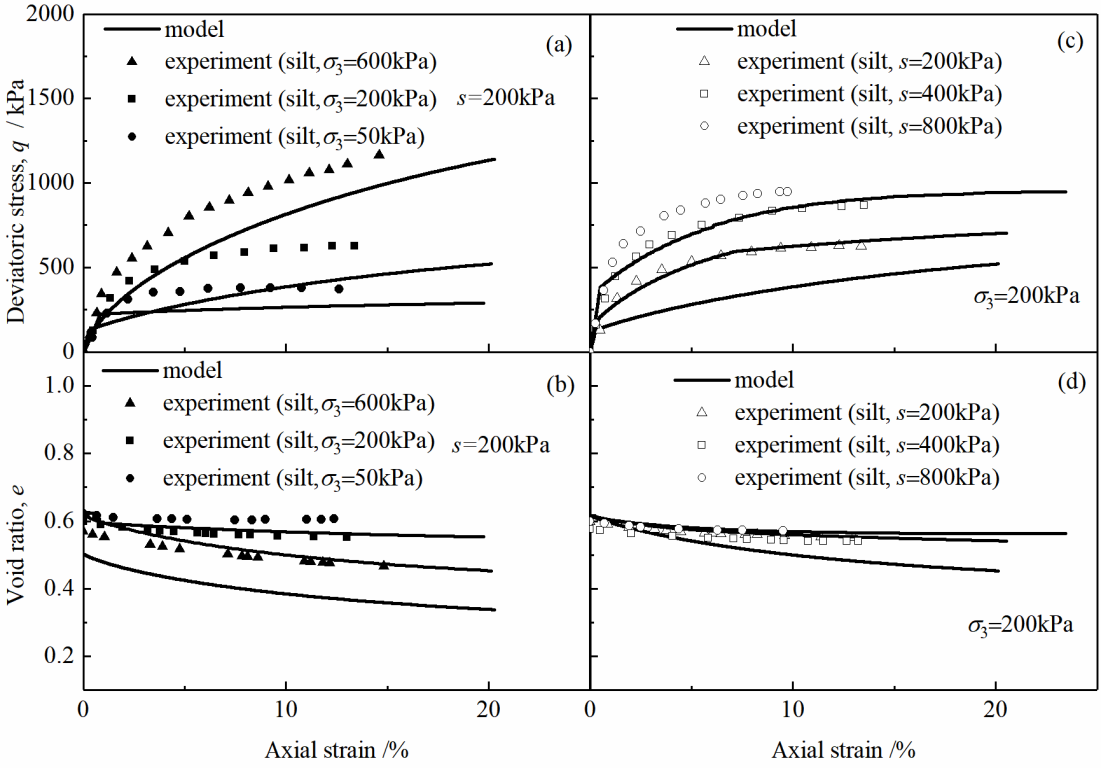

626

627 **Fig. 7.** Comparison between model results and experimental results on Jossigny silt

628 (Cui and Delage 1996) for shear at constant suction or cell pressure: (a/c) q; (b/d) e

629